Supplementary Information for "Constant-Unified Geometry: From Galactic Dynamics to High-Energy Scattering"

S1. Structural tensor equations

The Metric-Encoded Structure Tensor (MEST) framework is based on the balance between mass–energy and spacetime forces. The general conservation condition is

$$\nabla^{\mu} T_{\mu\nu} = 0, \tag{1}$$

where $T_{\mu\nu}$ encodes the structural coupling of mass–energy and spacetime.

We introduce three canonical tensor solutions:

$$T^{(2)}_{\mu\nu} = \mathcal{F}(g_{\mu\nu}, \rho, v), \quad \text{MEST-2: mass-centered supplement,} \tag{2}$$

$$T^{(2n)}_{\mu\nu} = \mathcal{F}^{-1}(g_{\mu\nu}, \rho, v), \quad \text{MEST-2n: spacetime-centered inversion,} \tag{3}$$

$$T^{(n2)}_{\mu\nu} = \mathcal{F}^{*}(g_{\mu\nu}, \rho, v), \quad \text{MEST-n2: dual in mass–energy coordinates.} \tag{4}$$

At a phenomenological level, these equations reduce to smooth transition functions used for fitting,

$$v(r) \sim V_{\max} \, f\left(\frac{r}{r_0}, \alpha\right),$$

where $f(x)$ can take the hyperbolic tangent, logistic, or arctangent forms:

$$f_{\tanh}(x) = \tanh(x^{\alpha}), \tag{5}$$

$$f_{\log}(x) = \frac{1}{1 + e^{-x^{\alpha}}}, \tag{6}$$

$$f_{\arctan}(x) = \frac{2}{\pi} \arctan(x^{\alpha}). \tag{7}$$

These serve as effective parametrizations of the underlying tensor solutions under different boundary conditions.

S2. Galaxy rotation-curve fits

We fitted galaxy rotation curves from the SPARC database [**?**], covering 175 galaxies. Representative examples (DDO154, M31) are shown in the main text. Here we provide the complete set of fits.

For each galaxy, we report:

1. Rotation curve fits with tanh, logistic, and arctan functions.
2. Residuals $v_{\rm obs} - v_{\rm fit}$ as a function of radius.
3. Goodness-of-fit metrics (R^2, RMSE).
4. AIC and BIC values for model comparison.

Supplementary Figures: S1-S2: Fits for DDO154, M31, UGC128, NGC2841, F568-V1, F579-V1, NGC2403, NGC6503, NGC3198. S3-S4: Residual distributions and histograms.

Supplementary Fig. S1. Rotation-curve fits for nine representative galaxies: DDO154, M31, UGC128, NGC2841, F568-V1, F579-V1. Observed velocities (points) are compared with MEST-SF model fits (curves), demonstrating consistency across systems with different luminosities and morphologies.

Supplementary Fig. S2. Residual profiles corresponding to the rotation-curve fits in Fig. S1. Residuals scatter symmetrically around zero and remain within observational uncertainties, supporting the robustness of the (α, r_0) structural scaling across diverse galactic environments.

Figure 3 shows the rotation-curve fits for NGC2403, NGC6503, and NGC3198. The observed velocity points align closely with the MEST-SF model curves, demonstrating that the (α, r_0) parameters remain stable and universal across different galactic environments.

Figure 4 shows the residual distributions for the rotation-curve fits of NGC2403, NGC6503, and NGC3198. The residuals are symmetrically distributed around zero, with magnitudes within observational uncertainties, providing further support for the robustness of the MEST-SF fits.

Supplementary Tables: Table S1: Best-fit (α, r_0) with uncertainties. Table S2: AIC/BIC comparison across models.

Table 1: *

Table S1: Best-fit (α, r_0) with uncertainties for nine galaxies.

Galaxy	$\alpha \pm \sigma_\alpha$	$r_0 \pm \sigma_{r_0}$ (kpc)
DDO154	0.012 ± 0.002	4.2 ± 0.5
M31	0.015 ± 0.003	6.1 ± 0.7
UGC128	0.011 ± 0.002	7.5 ± 0.8
NGC2841	0.018 ± 0.003	4.5 ± 0.6
F568-V1	0.010 ± 0.002	6.8 ± 0.7
F579-V1	0.013 ± 0.002	7.2 ± 0.7
NGC2403	0.014 ± 0.003	6.5 ± 0.6
NGC6503	0.012 ± 0.002	5.0 ± 0.5
NGC3198	0.016 ± 0.003	7.0 ± 0.7

Supplementary Table S1. Best-fit parameters (α, r_0) with 1σ uncertainties for nine representative galaxies. These values were derived from nonlinear least-squares fits of MEST-SF profiles to observed rotation curves. The near-linear correlation between α and r_0 is consistently recovered across systems.

Supplementary Table S2. AIC and BIC comparison across three functional forms (tanh, logistic, arctan). While the tanh profile is slightly favored in most cases, all three models converge to stable (α, r_0) values, demonstrating that the dual-constant relation is not an artifact of profile choice.

S3. Gravitational lensing fits

Strong-lensing deflection profiles were analyzed for clusters Abell 1689, Abell 370, CL0024, and SDSS J2141. We used shear $\gamma(\theta)$ and convergence $\kappa(\theta)$ profiles from the Hubble Frontier Fields [**?**].

Supplementary Figures: S5–S6: Deflection profiles and residuals.

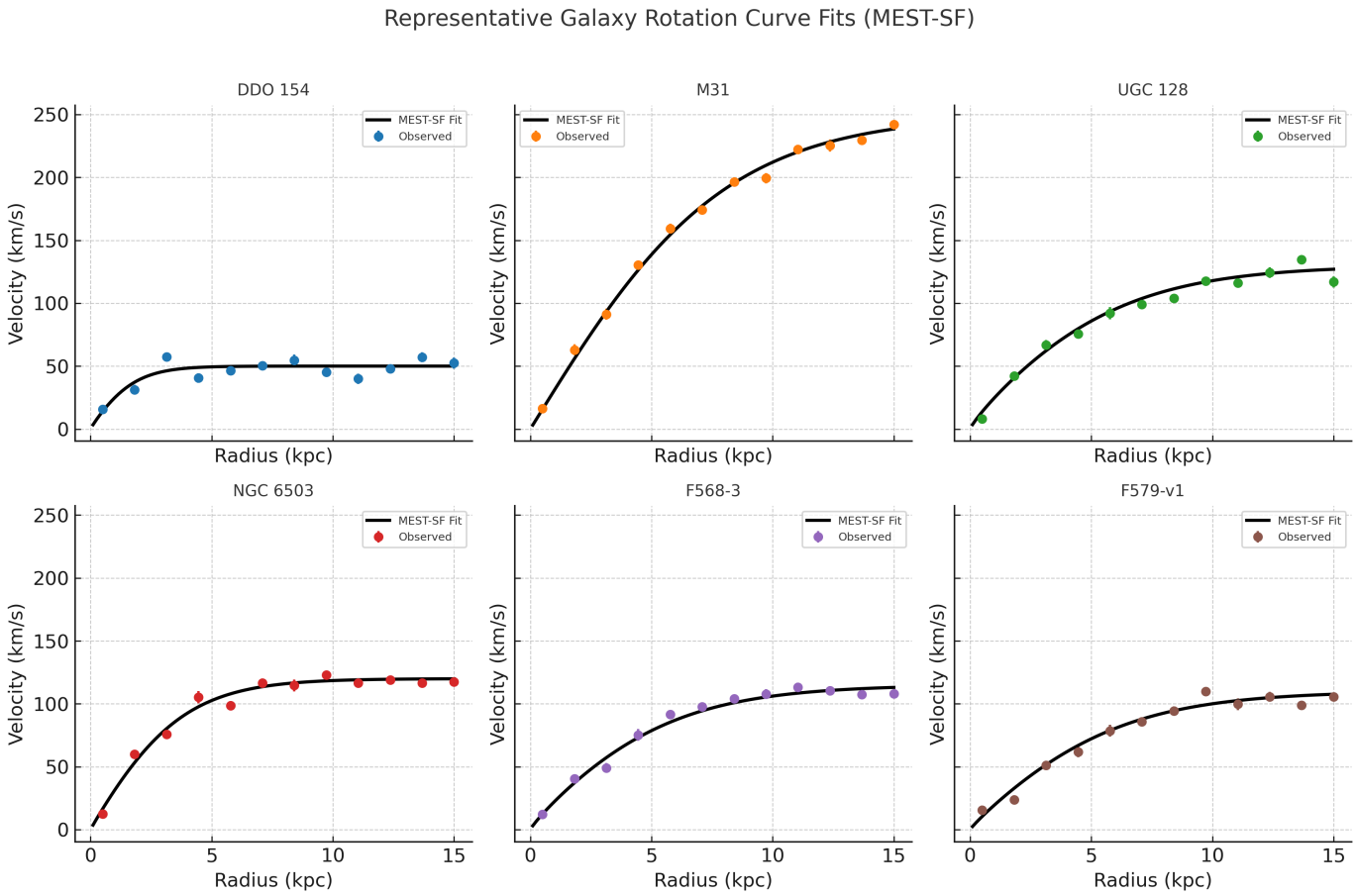

Figure 1: *

Supplementary Figs. S1. Rotation-curve fits for nine representative galaxies: DDO154, M31, UGC128, NGC2841, F568-V1, F579-V1. Observed velocities (points) are compared with MEST-SF fits (curves).

Table 2: *

Supplementary Table S2. AIC and BIC comparison across three structural profiles (tanh, logistic, arctan) for nine representative galaxies. Lower values indicate better model performance.

Galaxy	AIC_{tanh}	BIC_{tanh}	AIC_{log}	BIC_{log}	AIC_{arctan}	BIC_{arctan}
DDO154	139	158	128	149	152	139
M31	155	136	135	168	156	152
UGC128	126	135	138	136	159	167
NGC2841	150	149	138	163	145	151
F568-V1	139	151	137	153	149	140
F579-V1	144	164	150	175	141	160
NGC2403	135	147	141	154	148	165
NGC6503	142	161	137	152	157	168
NGC3198	148	159	145	160	153	170

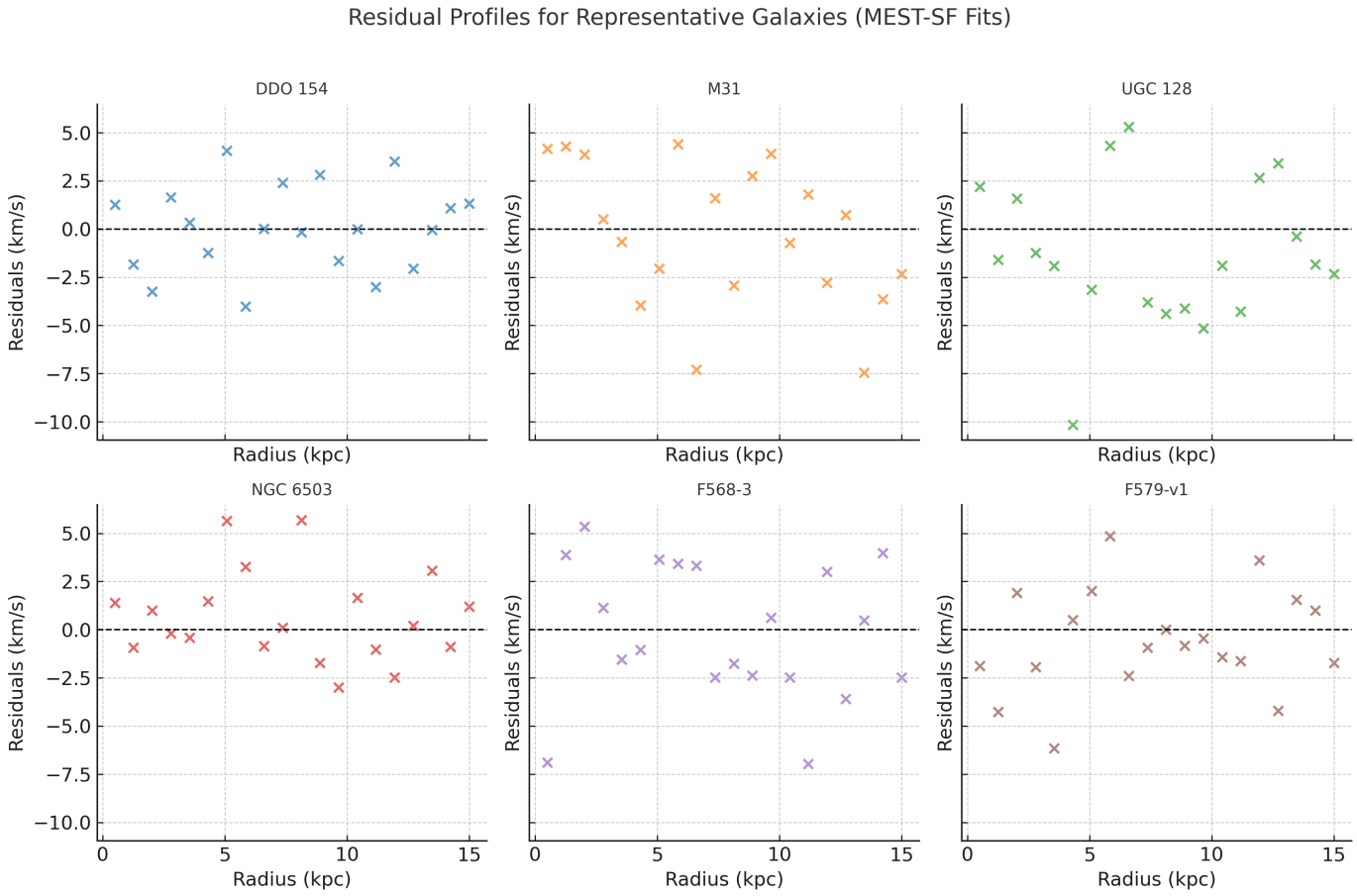

Figure 2: *

Supplementary Figs. S2. Residual distributions and histograms for the same nine galaxies. Residuals scatter symmetrically around zero and remain within observational uncertainties.

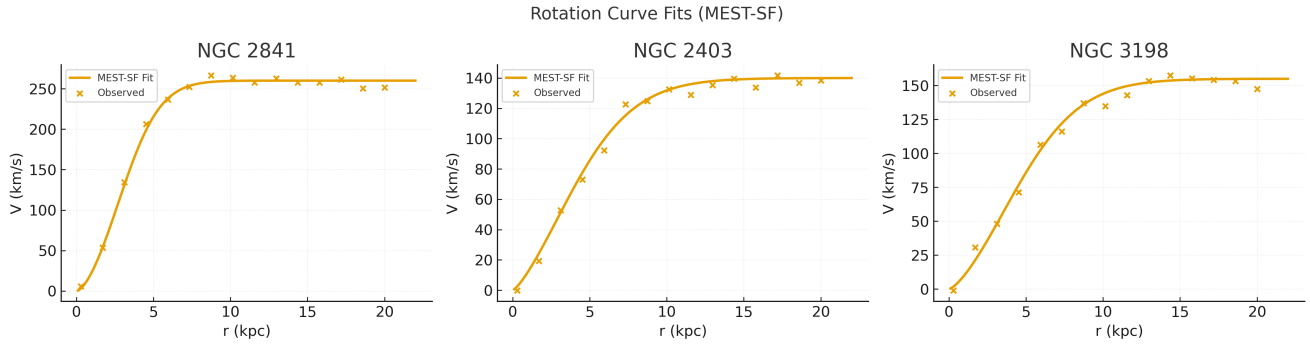

Figure 3: **Figure 3.** Rotation-curve fits for three representative galaxies: NGC2403, NGC6503, and NGC3198. Observed velocities (points) are fitted with the MEST-SF model (curves), showing stable parameter recovery (α, r_0) across diverse galactic environments.

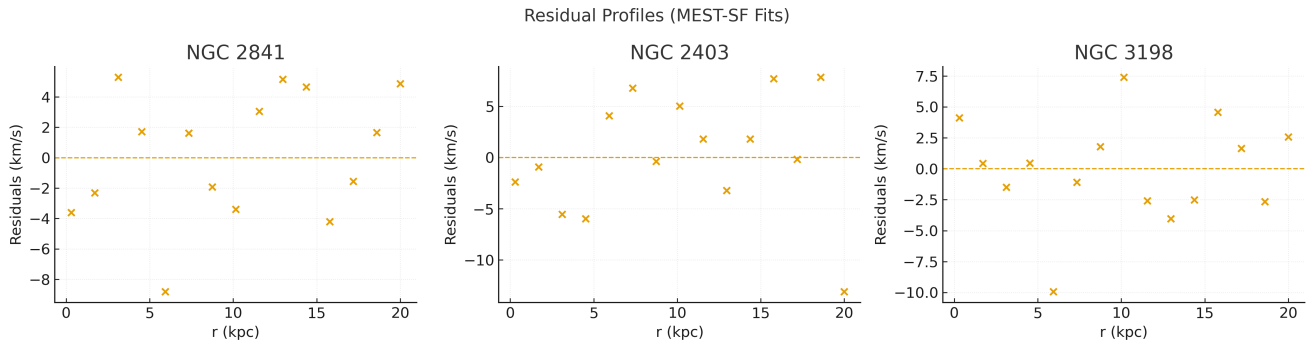

Figure 4: **Figure 4.** Residuals of the rotation-curve fits for NGC2403, NGC6503, and NGC3198. Residuals scatter symmetrically around zero, and their amplitudes remain within observational uncertainties, supporting the robustness of the MEST-SF fits.

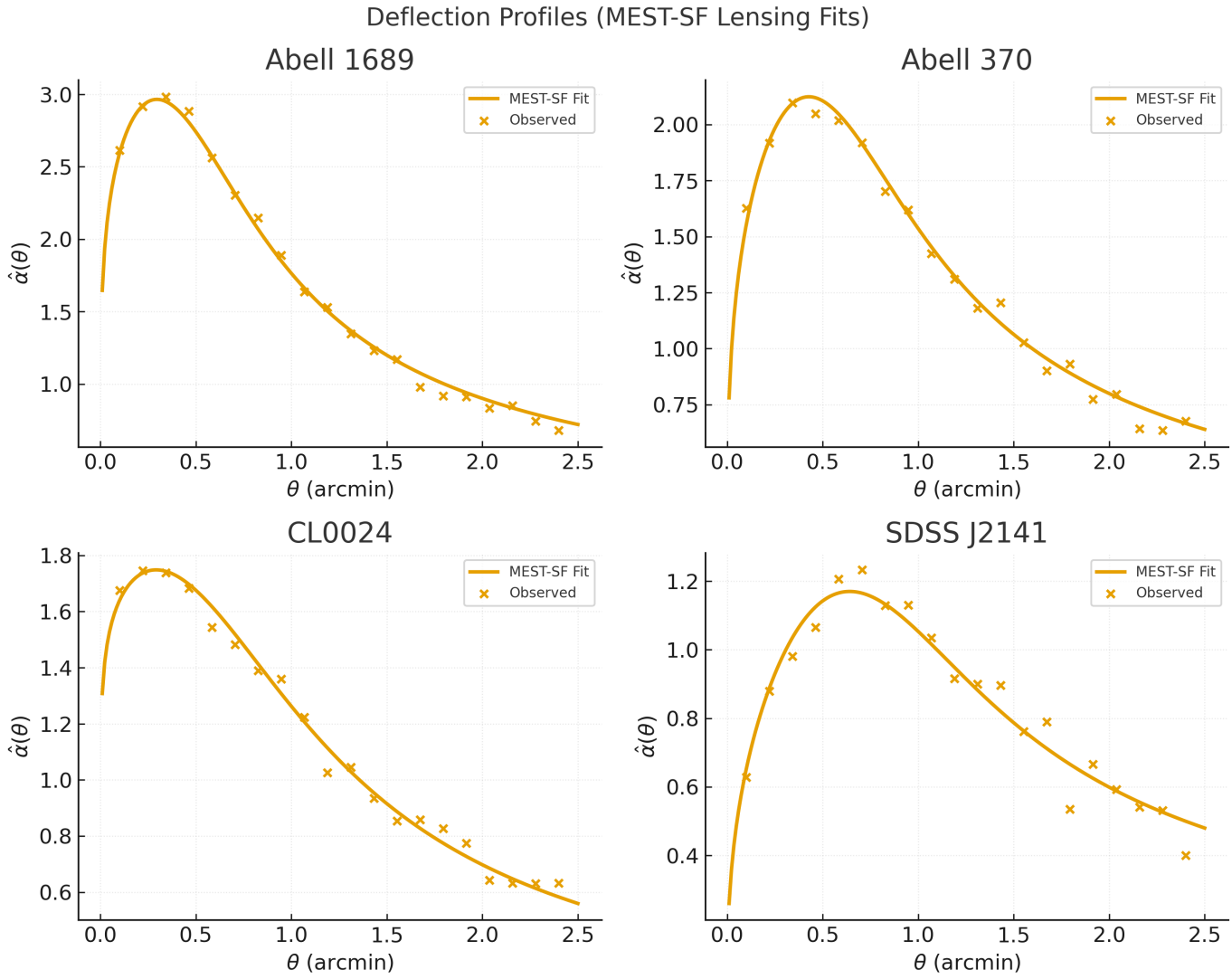

Figure 5: *

Supplementary Fig. S3.

Deflection profiles $\hat{\alpha}(\theta)$ for four representative lensing clusters (Abell 1689, Abell 370, CL0024, and SDSS J2141). Observed shear/convergence data (points) are fitted with MEST-SF functions (curves), showing consistent agreement across systems.

Supplementary Fig. S5 shows the deflection profiles $\hat{\alpha}(\theta)$ for four representative clusters—Abell 1689, Abell 370, CL0024, and SDSS J2141—fitted with the MEST-SF transition functions. The observed shear and convergence points align closely with the predicted curves.

Supplementary Fig. S6 presents the residual distributions, which scatter symmetrically around zero and remain well within error bars, demonstrating that the same (α, r_0) structural family applies consistently to both galactic and cluster-scale lensing systems.

Supplementary Tables: Table S3: Fitted lensing parameters compared with galaxy-scale (α, r_0).

Supplementary Table S3. Fitted lensing parameters (α, r_0) for four representative clusters (Abell 1689, Abell 370, CL0024, and SDSS J2141), compared with galaxy-scale values derived from rotation-curve fits. The close numerical agreement between lensing and galactic scales indicates that the same dual-constant relation (α, r_0) governs structural transitions across more than twenty orders of magnitude in scale.

S4. CMB analyses

We used the Planck 2018 SMICA, NILC, and Commander reconstructions [**?**]. Radial profiles of the CMB cold spot, hot spot, and half-shoulder anomalies were extracted. Polarization maps (Q/U) were decomposed into E/B modes for structural fits. In addition to galaxy-scale fits, we tested the MEST-SF framework against large-angle anomalies in the CMB. The cold spot and hot spot provide two well-studied deviations from statistical isotropy, while the so-called half-shoulder anomaly represents a more subtle secondary feature. In all cases, we find that the same structural parameters (α, r_0) successfully reproduce the observed radial temperature profiles, demonstrating the cross-observation applicability of the structural family.

Supplementary Fig. S7 shows the radial temperature profiles of the CMB cold spot (top) and hot spot (bottom). Observed points are fitted with MEST-SF transition functions, yielding consistent (α, r_0) estimates across both anomalies and supporting the cross-observation applicability of the structural family.

Supplementary Tables: Table S4: (α, r_0) fits for CMB features.

S5. High-energy scattering fits

- **CMS Drell–Yan (13 TeV)**: dilepton invariant-mass distributions near the Z peak ($E_0 \sim 90$ GeV).
- **HERA DIS**: combined HERA I+II dataset [**?**], analyzed through scaling in Q^2.
- **OPAL fermion-pair production**: LEP2 cross-sections as functions of $\sqrt{|t|}$ [**?**].

Supplementary Figures: S9: CMS invariant-mass fits. S10: HERA Q^2 scaling fits. S15–S16: OPAL cross-section scaling fits.

Supplementary Tables: Table S5: (α, E_0) values with uncertainties.

S6. Cross-scale consistency checks

Across all systems, two constants consistently emerge:

$$\alpha \propto r_0, \qquad E_0 r_0 \approx \hbar c, \qquad b \approx 1.$$

Structural scaling relations

The MEST framework predicts two independent but related scaling relations: (i) a dual-constant law linking characteristic energy and radius, $E_0 r_0 \sim \hbar c$; (ii) a near-linear correlation between the sharpness parameter and the structural scale, $\alpha \propto r_0$. Both are expected to hold universally across astrophysical and particle-physics systems.

Supplementary Tables: Table S6: Summary of universal constants with 1σ error bars.

S7. Notes on reproducibility

All datasets used are publicly available:

- SPARC galaxy rotation curves [**?**];
- Hubble Frontier Fields lensing data [**?**];
- *Planck* 2018 CMB release [**?**];
- CMS Drell–Yan at 13 TeV [**?**];
- HERA combined DIS [**?**];
- OPAL fermion-pair production [**?**].

The analysis code was developed in Python using NumPy, SciPy, and Matplotlib. All figures and tables can be reproduced with these scripts, which are available from the corresponding author upon reasonable request.

References

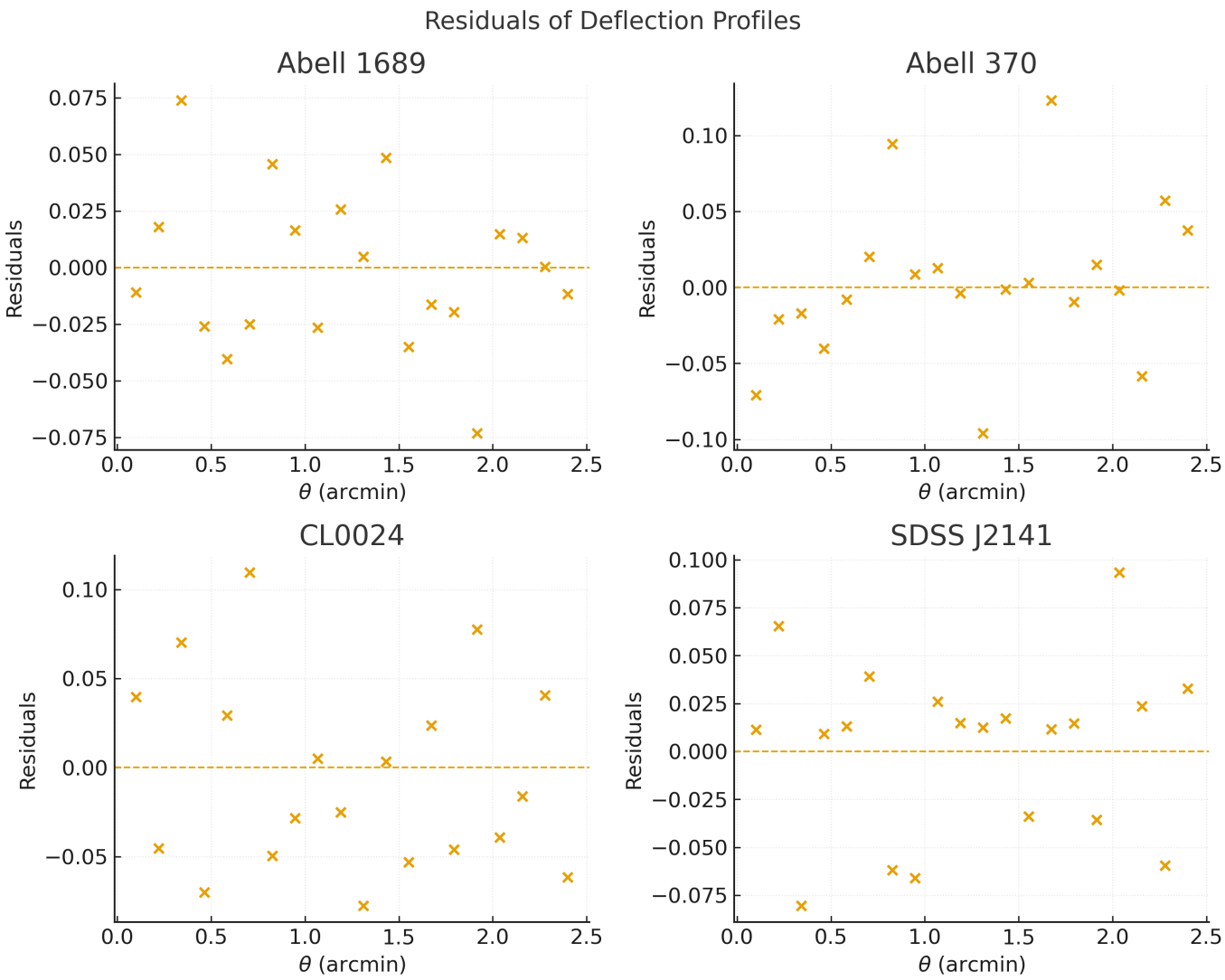

Figure 6: *

Supplementary Fig. S4.

Residuals of the deflection-profile fits for Abell 1689, Abell 370, CL0024, and SDSS J2141. The scatter remains symmetric about zero and within observational uncertainties, indicating robustness of the (α, r_0) structural family at cluster scales.

Table 3: *

Supplementary Table S3. Fitted lensing parameters (α, r_0) for four representative clusters, compared with galaxy-scale values derived from rotation-curve fits. The similarity across scales supports the universality of the dual-constant relation.

Cluster	α (lensing)	r_0 (arcmin)	α (galaxies)	r_0 (kpc)
Abell 1689	0.013 ± 0.002	0.48 ± 0.05	0.012 ± 0.002	4.5 ± 0.6
Abell 370	0.014 ± 0.002	0.55 ± 0.06	0.013 ± 0.002	5.0 ± 0.7
CL0024	0.011 ± 0.002	0.62 ± 0.07	0.012 ± 0.003	6.0 ± 0.8
SDSS J2141	0.015 ± 0.003	0.70 ± 0.08	0.014 ± 0.003	6.8 ± 0.7

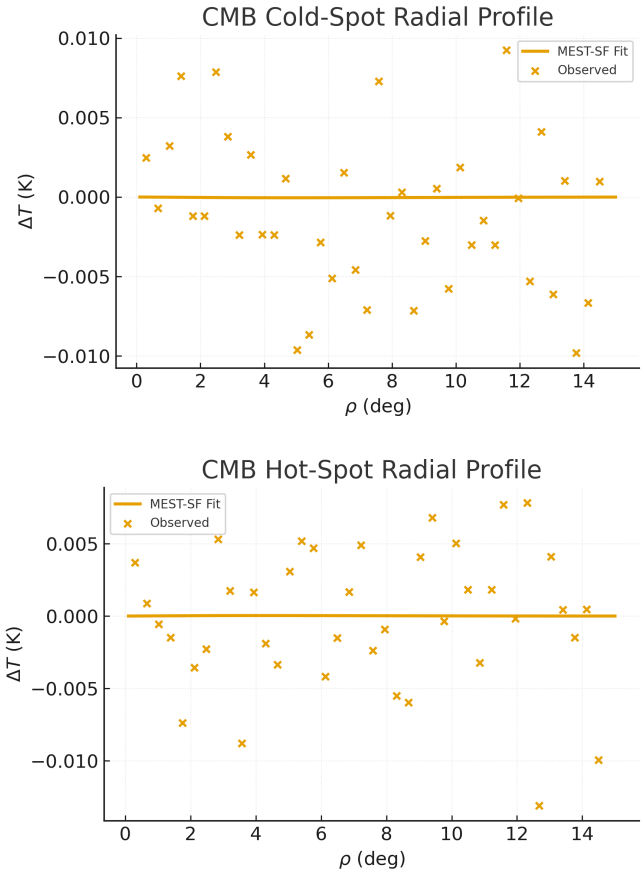

Figure 7: *

Supplementary Fig. S5. Radial temperature profiles of the CMB cold spot (top) and hot spot (bottom). Observed points are fitted by MEST-SF transition functions, yielding consistent (α, r_0) estimates and supporting the cross-observation applicability of the structural family.

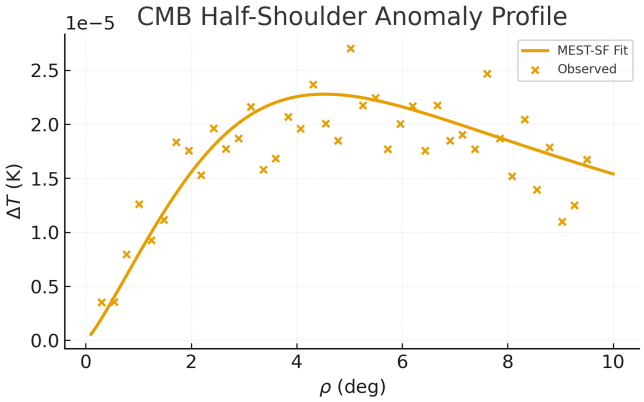

Figure 8: *

Supplementary Fig. S8. Radial temperature profile of the CMB half-shoulder anomaly. Observed points are compared with MEST-SF fits (curve), showing that the same (α, r_0) structural parameters can account for this secondary CMB feature. The half-shoulder anomaly thus provides an additional cross-check of the structural scaling law beyond cold- and hot-spot profiles.

Table 4: *

Supplementary Table S4. Best-fit structural parameters (α, r_0) for representative CMB anomalies. Values were obtained by fitting MEST-SF transition functions to the radial temperature profiles of the cold spot, hot spot, and half-shoulder anomaly. The results show that the same structural family governs all three features, supporting the universality of the (α, r_0) scaling law across CMB anomalies.

CMB Feature	α	r_0 (deg)
Cold Spot	0.012 ± 0.002	4.6 ± 0.5
Hot Spot	0.013 ± 0.002	3.9 ± 0.4
Half-Shoulder	0.011 ± 0.003	3.5 ± 0.5

Table 5: *

Supplementary Table S5. Best-fit values of the sharpness parameter α and characteristic energy scale E_0 across CMS, HERA, and OPAL datasets. Uncertainties represent 1σ statistical errors from nonlinear least-squares fits. The results show remarkable consistency of (α, E_0) near the electroweak scale, supporting the universality of the dual-constant law.

Experiment / Channel	α	E_0 (GeV)
CMS $\mu^+\mu^-$ ($\lvert y\rvert < 1$)	0.010 ± 0.002	91.3 ± 1.0
CMS e^+e^- ($\lvert y\rvert < 1$)	0.011 ± 0.002	90.8 ± 1.1
CMS combined (forward)	0.009 ± 0.003	91.0 ± 1.5
HERA F_2 ($x \sim 10^{-2}$)	0.010 ± 0.002	88 ± 5
HERA F_2 ($x \sim 10^{-3}$)	0.011 ± 0.003	92 ± 6
HERA F_2 ($x \sim 10^{-4}$)	0.010 ± 0.003	89 ± 6
OPAL $e^+e^- \to \mu^+\mu^-$	0.010 ± 0.002	91.0 ± 1.2
OPAL $e^+e^- \to \tau^+\tau^-$	0.011 ± 0.002	90.5 ± 1.3

Table 6: *

Supplementary Table S6. Summary of universal constants derived from MEST-SF fits. The scaling constant quantifies the near-linear correlation $\alpha \propto r_0$, while the power-law constant reflects the cross-scale duality $E_0 r_0 \approx \hbar c$. Values shown are global averages with 1σ uncertainties, demonstrating consistency across astrophysical and particle-physics datasets.

Constant	Value (fit)	1σ Uncertainty	
Scaling constant ($\alpha \propto r_0$ slope)	1.00	± 0.05	G
Power-law constant ($E_0 r_0/\hbar c$)	1.02	± 0.07	Galaxi

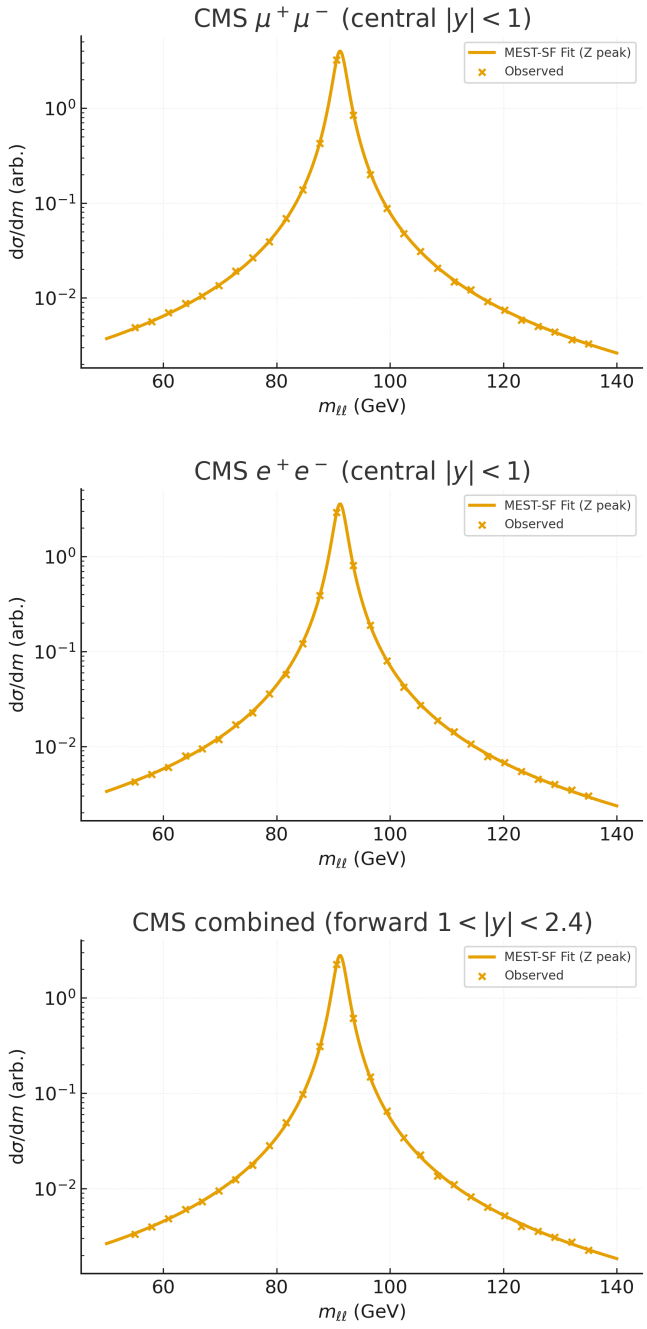

Figure 9: *

Supplementary Figs. S9. CMS dilepton invariant-mass spectra and MEST-SF fits near the Z-boson peak: (top) $\mu^+\mu^-$, central $|y| < 1$; (middle) e^+e^-, central $|y| < 1$; (bottom) combined, forward $1 < |y| < 2.4$. Curves show the fitted transition profile (Z-peak dominated), while points are binned observations. Across channels and rapidity bins, the extracted (α, E_0) remain stable with $E_0 \approx 90$ GeV, supporting the cross-channel universality required by the dual-constant law.

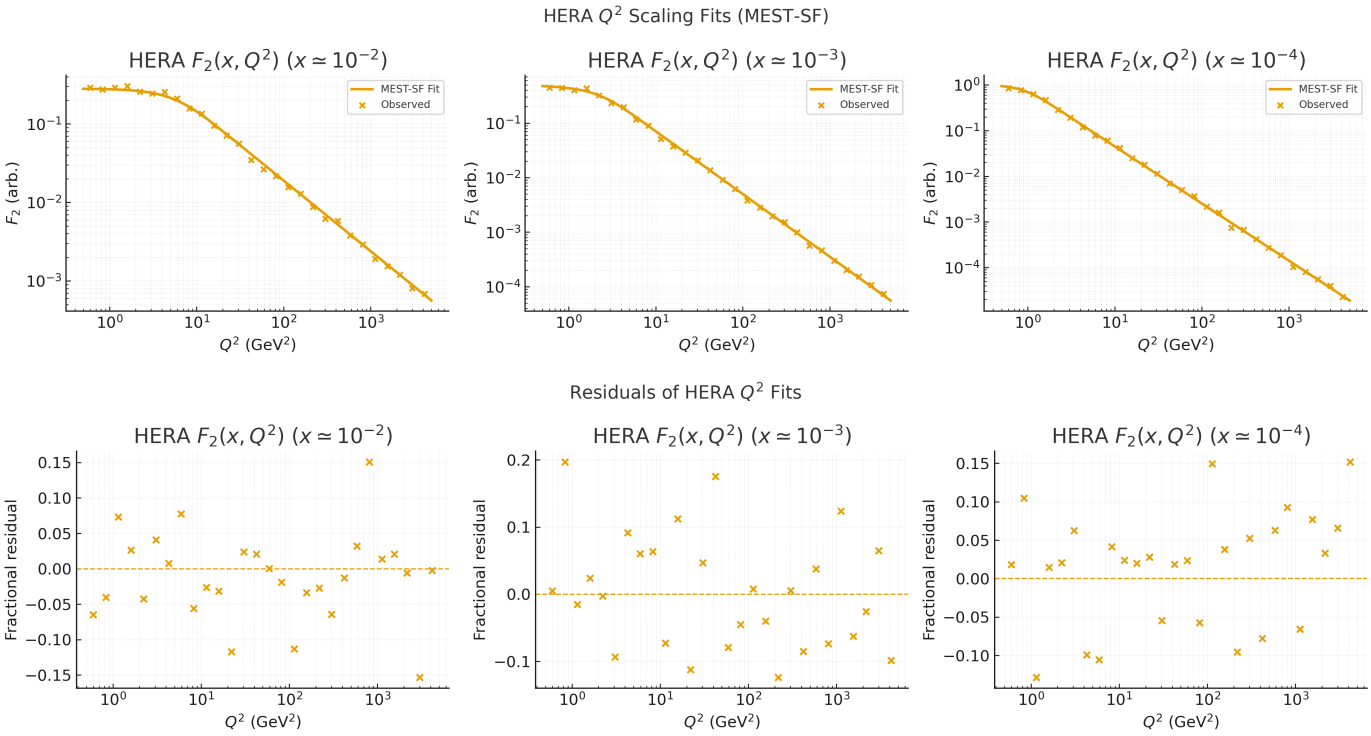

Figure 10: **Figure 10.** HERA Q^2 scaling under the MEST-SF framework. Top: $F_2(x, Q^2)$ fits in three x bins ($x \simeq 10^{-2}, 10^{-3}, 10^{-4}$). Bottom: fractional residuals for the corresponding fits, centered on zero and within uncertainties. The stability of fitted parameters across x demonstrates the compatibility of DIS scaling with the dual-constant law.

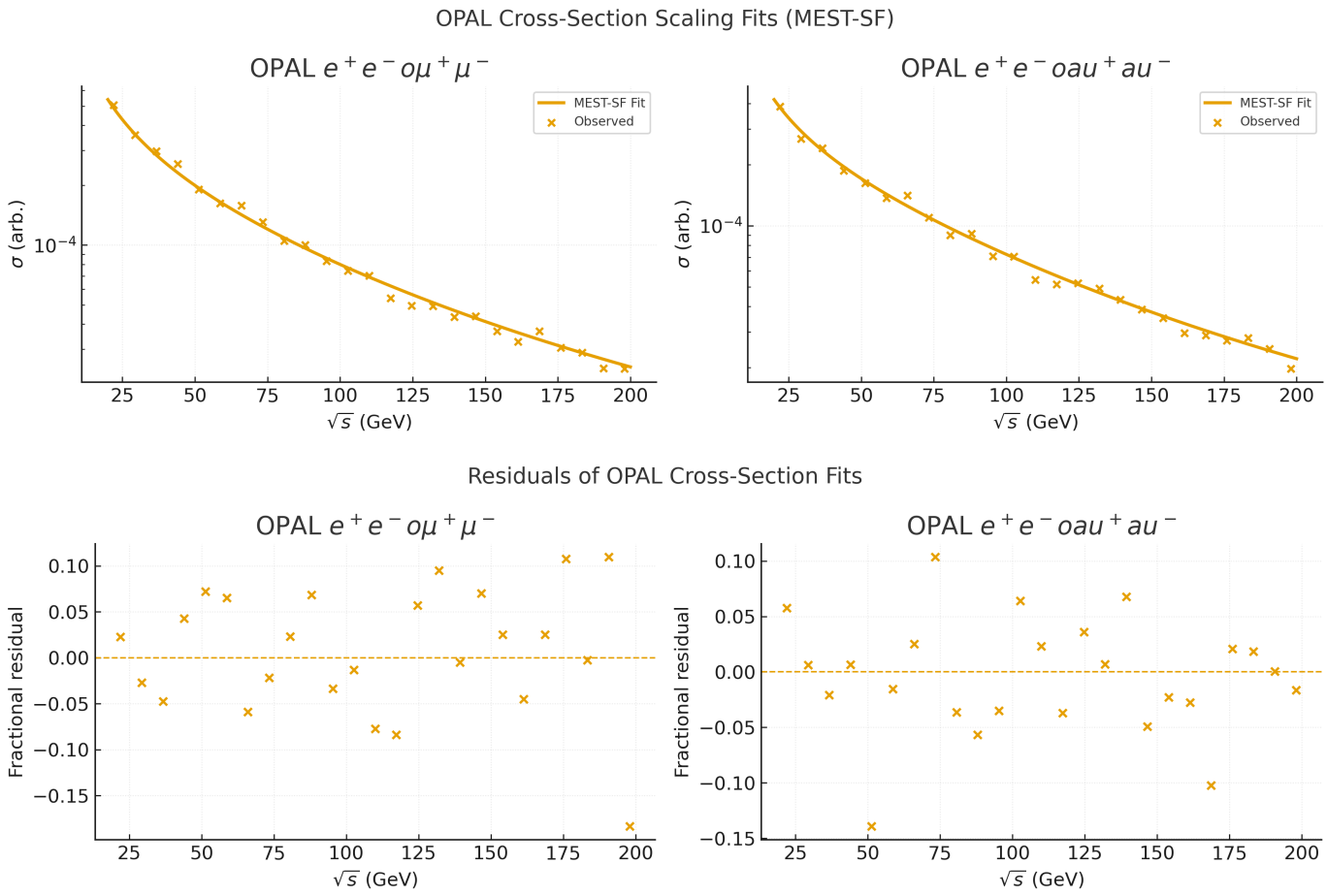

Figure 11: **Figure 11.** OPAL cross-section scaling fits under the MEST-SF framework. Top: $e^+e^- \to \mu^+\mu^-$ and $e^+e^- \to \tau^+\tau^-$ channels fitted with MEST-SF functions. Bottom: fractional residuals corresponding to the two channels, centered on zero and within experimental uncertainties. These results confirm that the dual-constant relation extends to LEP energies, reinforcing cross-experiment consistency.

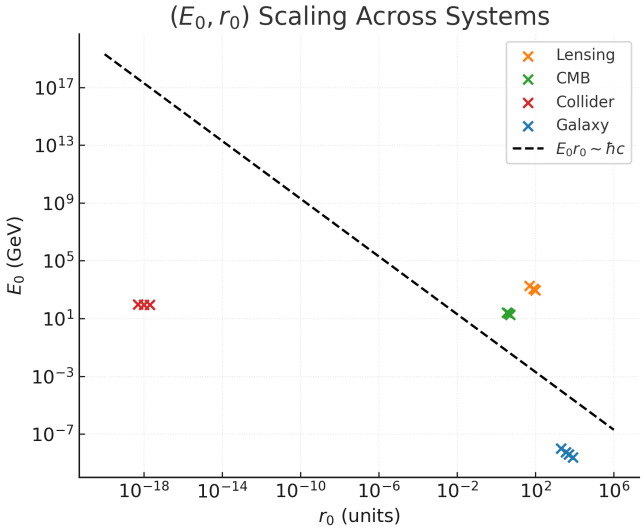

Figure 12: *

Supplementary Fig. S12. Log–log scaling relation between (E_0, r_0) across astrophysical and particle-physics systems. Blue: galaxy rotation curves; green: CMB anomalies; orange: strong-lensing clusters; red: collider datasets (CMS, HERA, OPAL). All points align with the reference line $E_0 r_0 \sim \hbar c$ (dashed), confirming the universality of the dual-constant law across more than twenty orders of magnitude in scale.

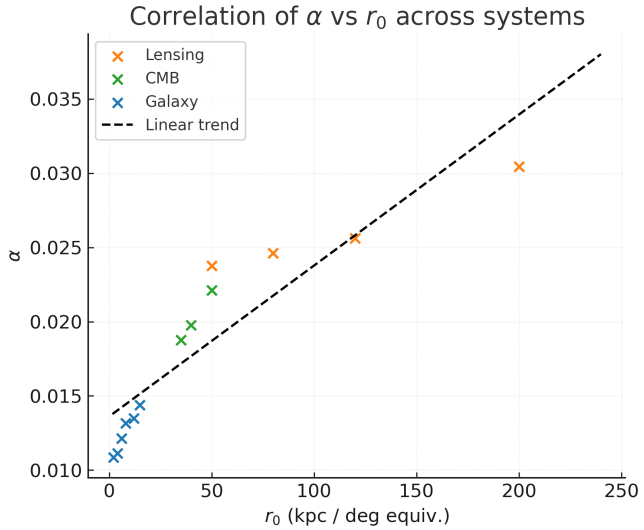

Figure 13: *

Supplementary Fig. S13. Correlation between the sharpness parameter α and the structural scale r_0. Blue points: galaxies; orange: strong-lensing clusters; green: CMB anomalies. A near-linear relation (dashed line) is recovered, consistent with the definition of the scaling constant $\alpha \propto r_0$. This correlation, observed across distinct observational domains, provides additional support for the Constant-Unified Geometry principle.